Improving a convection-permitting model simulation of a cold air outbreak

RMetS
Royal Meteorological Society

Improving a convection-permitting model simulation of a cold air outbreak

P. R. Field,[a]*R. J. Cotton,[a] K. McBeath,[a] A. P. Lock,[a] S. Webster[a] and R. P. Allan[b]
[a]*Met Office, Exeter, UK*
[b]*Department of Meteorology, University of Reading, UK*

*Correspondence to: P. R. Field, Met Office, FitzRoy Road, Exeter EX1 3PB, UK.
E-mail: paul.field@metoffice.gov.uk

A convection-permitting local-area model was used to simulate a cold air outbreak crossing from the Norwegian Sea into the Atlantic Ocean near Scotland. A control model run based on an operational configuration of the Met Office UKV high-resolution (1.5 km grid spacing) NWP model was compared to satellite, aircraft and radar data. While the control model captured the large-scale features of the synoptic situation, it was not able to reproduce the shallow (<1.5 km) stratiform layer to the north of the open cellular convection. Liquid water paths were found to be too low in both the stratiform and convective cloud regions. Sensitivity analyses including a modified boundary-layer diagnosis to generate a more well-mixed boundary layer and inhibition of ice formation to lower temperatures improved cloud morphology and comparisons with observational data.

Key Words: Unified Model; mixed phase; boundary layer

Received 28 April 2012; Revised 13 December 2012; Accepted 20 December 2012; Published online in Wiley Online Library 17 April 2013

Citation: Field PR, Cotton RJ, McBeath K, Lock AP, Webster S, Allan RP. 2014. Improving a convection-permitting model simulation of a cold air outbreak. *Q. J. R. Meteorol. Soc.* **140**: 124–138. DOI:10.1002/qj.2116

1. Introduction

Convection-permitting models are being used routinely for operational numerical weather prediction (NWP). This approach can provide realistic realisations of convective events, their mesoscale organisation and propagation (Lean *et al.*, 2008). Cold air outbreaks are challenging for such models because the depth of the boundary layer and the scale of the convection is approaching the resolution of the model. In addition, any cloud liquid is usually supercooled and so the accurate treatment of mixed phase by the model is likely to be important. Cold air outbreaks are a common phenomena around the United Kingdom. These potentially multi-day events can bring snow, and the accuracy of a forecast will depend on the success of the simulation.

The case presented in this article is a cold air outbreak which was observed on 31 January 2010. These outbreaks are a common feature in the wintertime to the north of the British Isles where cold air from the polar cap sweeps off the ice edge over open water. The convection often originates as organised rolls near to the ice edge but eventually changes into open cellular convection as the boundary layer evolves (Brümmer and Pohlmann, 2000, and references therein). These cloud morphological changes can have important impacts on the transport of heat and moisture as well as radiative effects such as high-latitude short-wave errors that are one of the largest biases in climate models (Trenberth and Fasullo, 2010; Karlsson and Svensson, 2011; Bodas-Salcedo *et al.*, 2012). Accurate forecasts of such events are also important for civil aviation safety (e.g. Wilkinson *et al.*, 2012).

Previous high-resolution modelling studies of cold air outbreaks show roll formation and generally exhibit a boundary-layer thickness of less than 1 km (e.g. Gryschka and Raasch, 2005; Liu *et al.*, 2006). Both studies were idealised and concentrated on the early development of the cloudy boundary layer. The former study used a model capable of a multi-phase representation of water, while the second study did not have a cloud ice representation.

Larger-domain mesoscale modelling studies (e.g. Wacker *et al.*, 2005; 7 km grid resolution) of cold air outbreaks found broadly good agreement between modelled and observed boundary-layer structure, but the coarse grid resolution meant that the smaller-scale convection remained unresolved.

A model intercomparison study looked at the performance of a variety of single-column and cloud-resolving models in the stratiform region of a cold air outbreak during the Mixed-Phase Arctic Cloud Experiment (Klein *et al.*, 2009). For that case, the boundary layer was 1–1.5 km deep (−15 °C at the top). Observed cloud liquid water paths (LWPs) were between 0.1 and 0.2 kg m^{-2}, while ice water paths were likely between 0.01 and 0.03 kg m^{-2} . Some models with complex microphysics were able to reproduce the LWP, but other models which produced low LWPs were able to increase this value only when ice processes were disabled. This led to the conclusion that there was excessive conversion of liquid to ice. Similar conclusions about the trade-off between ice processes and LWP have been made by others studying Arctic stratus cloud (e.g. Morrison and Pinto, 2006; Liu *et al.*2011).

The aim of this study is to compare a high-resolution weather model simulation of a real case to *in situ* and remote-sensing observations. This was done for a situation which is challenging to the model in terms of the grid resolution employed and the physics parametrizations. This case covers the evolution of a completely cloud-covered shallow boundary layer through a transition to open-celled convection. Changes to the physics representations will be made based on problems highlighted through comparison with the data. Finally, it will be determined if any of the changes which could easily be implemented in an operational forecast model could lead to an improved forecast.

2. Observations

2.1. Satellite data

Microwave-based retrievals of LWP, integrated water vapour (WVP) and sea surface temperature (SST) are available from the AMSR-E (Advanced Microwave Scanning Radiometer) sensor on the AQUA/TERRA polar orbiting platforms. For this geographical region, the data may suffer from systematic biases of the order of 15% (O'Dell *et al.*, 2008), mainly due to assumptions about partitioning of rain and cloud water. The LWP product is produced by Remote Sensing Systems (RSS) on a 0.25° grid and has an accuracy of 0.025 kg m^{-2} (Wentz and Spencer, 1998). Horvath and Davies (2007) show agreement within 10% between LWP obtained using the Wentz and Spencer (1998) product and other satellite measurements for boundary-layer cloud with large cloud fractions, but note a positive bias for lower cloud fractions. The overpass presented for this day occurred at 1255 UTC. Top-of-atmosphere outgoing short-wave (SW) and long-wave (LW) broadband radiative flux estimates are provided by the CERES (Clouds and the Earth's Radiant Energy System) instrument Single Scanner Footprint (SSF) processing system (version SSF_Aqua-FM3-MODIS_Version2F_008017) described in Wielicki *et al.*(1996). For overcast, moderate or thick low clouds over the ocean, Loeb *et al.*(2007) estimate an uncertainty in radiance to flux conversion of less than 5% for SW and less than 3% for LW. Given typical SW fluxes of up to 200 W m^{-2} and LW fluxes of around 200 W m^{-2} for the period of study, from the above uncertainty estimates we consider an accuracy of 10 W m^{-2} for SW fluxes and 6 W m^{-2} for the LW flux to be reasonable.

There was a MODIS (Moderate Resolution Imaging Spectroradiometer) overpass at 1235 UTC on 31 January. MODIS level 2 data (http://ladsweb.nascom.nasa.gov/) provide retrievals of cloud-top pressure, cloud-top temperature, optical thickness and droplet effective radius. At this time of the year, the solar zenith angle is large (∼80°) and so there is a potential for bias in these retrievals.

2.2. Aircraft instrumentation

Observations presented here, from a flight on 31 January 2010, were from the FAAM (Facility for Airborne Measurement) BAe-146 aircraft (http://www.faam.ac.uk/index.php/science-instruments provides details of standard meteorological measurements such as wind, temperature and pressure). Instrumentation included a hot-wire deep cone Nevzorov probe (Korolev *et al.*, 1998) to mitigate problems with bouncing (Korolev *et al.*, 2011) and a new calibration technique to provide condensed total water estimates to an accuracy of 0.001 g m^{-3} (Cotton *et al.*, 2012); this saturates at ∼1 g m^{-3} (although it is noted that measured values during this flight did reach 2 g m^{-3}). The Nevzorov probe provided *in situ* ice water content (IWC) estimates. Cloud droplet number and sizing (2–50 μm) were provided by the laser-scattering Cloud Droplet Probe (CDP, Droplet Measurement Technologies, USA). The CDP was used to provide *in situ* liquid water content (LWC) estimates and was found to show good agreement with a liquid water hot-wire probe. Ice crystals were measured using a Particle Measuring Systems 2D-C (25–800 μm) with modified tips (Korolev *et al.*, 2011) and interarrival time filtering (Field *et al.*, 2006) to reduce the effects of shattering on the measured size distribution. A Droplet Measurement Technologies CIP-100 was used for larger particles (100microns-6mm). Ice properties such as ice number concentration were derived only from particles larger than 100 μm due to uncertainties with measuring and counting smaller particles. A Buck Research Instruments chilled mirror hygrometer provided relative humidity information.

2.3. Radar data

Radar data from the 3 GHz (C-Band) UK operational radar located at Stornoway was used to compare with model data as described by McBeath *et al.*(2012) which included clustering and tracking of cells. Model and radar data within 150 km of 58.2°N, 6.2°W and 0930–1400 UTC were processed. Combining radar data from four scan angles provided composite reflectivity fields at an altitude of ∼2 km regridded onto the same resolution grid as the model data. A threshold of 10 dBZ was applied to the radar and model-derived reflectivity fields at this height, and histograms of convective cell size and shape were derived. For the radar data, an individual convective cell is defined by a closed 10 dBZ reflectivity contour. Each identified convective cell is enclosed by the smallest fitting circle. The diameter of this circle defines the convective cell size and the fraction of the circle occupied by the area enclosed by the 10 dBZ contour is termed the fill fraction.

3. Unified Model

The Unified Model is used at a variety of scales for climate prediction and NWP. The data presented here are from a nested high-resolution model based on an operational UKV configuration (vn7.7, Parallel Suite 26). The global model (N512; 25 km grid spacing at midlatitudes) was nested down through 12 km, 4 km and 1.5 km gridscale configurations of the UM. The 1.5 km domain was 750 km (east–west) by 1500 km (north–south). In the vertical there are 70 levels stretching up to 40 km (52 below 10 km, 33 below 4 km, 16 below 1 km) and the time step is 50 s. Lateral boundary conditions are updated at 1 h intervals to the 12 and 4 km nests and at 0.5 h intervals to the 1.5 km nest. There is no convection scheme in the 4 and 1.5 km grid-scale models; the model handles convection at the grid scale.

Mixing is handled in the vertical by a non-local 1D boundary-layer scheme. Lock *et al.*(2000) describe the boundary-layer scheme in the UM which generates a diagnosis of boundary-layer 'type' based on the surface buoyancy flux and profiles of potential temperature, winds and humidity. The boundary-layer type determines the non-local mixing throughout the lower troposphere. If the environment is diagnosed to be conditionally unstable (i.e. capped by cumulus clouds), then vertical mixing in the cloud layer is assumed to be resolved and the boundary-layer parametrization mixes only to the lifting condensation level (Lock, 2011, provides full documentation.)

The Unified Model cloud microphysics is a single-moment three-phase representation. For the liquid phase there are prognostic variables for cloud water and rain mixing ratio. For ice there is a prognostic variable for snow mass mixing ratio that represents all ice in the grid box. Production of cloud water is through condensation and loss occurs through droplet settling, autoconversion of droplets to rain, freezing of droplets by ice nucleation and riming. Production of rain mixing ratio is via autoconversion, accretion and melting of ice. Loss of rain mixing ratio is from evaporation, capture by ice and homogeneous ice nucleation. Sedimentation can lead to loss or gain of rain. Ice mixing ratio production is from diffusional growth, capture of rain and riming. Loss of ice mixing ratio comes from sublimation and melting. Sedimentation acts on the ice mixing ratio. The basic formulation is described by Wilson and Ballard (1999) and fuller documentation by Wilkinson (2011).

Of direct interest here is that heterogeneous ice nucleation occurs when the temperature is lower than $-10\,^{\circ}$C and liquid water is present. The control snow size distribution representation is an exponential distribution based on the Houze *et al.*(1979) observations. There is an additional diagnostic split of the ice mixing ratio between ice crystals and snow which is a function of the depth below cloud top. This provides a steeper distribution of small crystals which sediment slower (Cotton *et al.*, 2012, provide a fuller description). At each time step, the ice mixing ratio is diagnosed into 'ice' and 'snow', the process rates are computed for each, and then they are summed to provide the combined effect.

A cloud scheme deals with sub-grid humidity variations (Smith, 1990). The model is non-hydrostatic and uses a semi-Lagrangian dynamical formulation (Cullen *et al.*, 1997; Davies *et al.*, 2005). For the liquid phase, the radiation scheme assumes a constant droplet number ($100\,\mathrm{cm}^{-3}$ over ocean) and combines this with the liquid water content to compute an effective radius for use in the SW calculations. For the LW, a constant effective radius of 7 μm for droplets is assumed. There is also a heterogeneity factor (0.7) to account for the effects of cloud structure on the radiation field. More details of the Unified Model can be found in Walters *et al.*(2011) and references therein, including details about the global model analysis used to initialise this case-study. The data presented here are from a run initialised from archived global analyses at 1200 UTC on 30 January 2010. The 1.5 km nested run began 6 h later and runs from 1800 UTC on 30 January through to the end of 31 January 2010. The comparisons are made with observations during 31 January.

4. Results

4.1. Comparison with control model

In this section the observations are introduced and compared to the control model (**h**). Based on any deficiencies identified, changes to the microphysical representation were made and their similarity to the observations is discussed. It was noted that the position of synoptic features at 1300 UTC was better matched to the model at 1100 UTC. Therefore, for the comparisons of WVP and LWP those times were used. For the SW and LW, 1200 UTC was used.

4.1.1. Synoptic situation

Figure 1 shows the 1200 UTC analysis for 31 January 2010. This general synoptic pattern persisted from 29 January until 1 February. There was a strong northerly flow extending from latitudes higher than 70°N to the southern tip of the British Isles. A polar low feature was present near 68°N, 4°E (location in Figure 2(b)) which constricted the flow to the east of Iceland. Further into the Atlantic, there was a warm front to the southwest of Iceland which had a cirrus shield ahead of it. The large-scale sea-level pressure pattern is very similar to the composite produced by Kolstad *et al.*(2009) for strong marine cold air outbreaks in this region. MODIS radiance imagery from a visible channel 4 (545–565 nm, Figure 2(a)) and infrared channel 31 (10.78–11.28 μm, Figure 2(b)) shows the overrunning cirrus from this warm front. This cirrus can be seen as lighter regions in Figure 2(b) to the west of the 12°W meridian. North of 64°N, the cirrus extends further eastwards to 6°W. The polar low is a clear cyclonic feature in the cloud fields. In the area bounded by 12–6°W and 60–64°N, there is low cloud exhibiting nearly complete cloud cover. South of this, the cloud breaks up into open cellular convection.

4.1.2. Satellite comparison

Examination of the performance of the control model (Figure 2(c)) shows that it exhibits gross similarities with the satellite-observed cloud morphology (Figure 2(a, b); irradiance and radiances are compared only to assess the gross cloud structures). The incoming cirrus shield, polar low and open cellular convection near Scotland are captured, but the stratiform cloud with cloud fraction close to 100% between the polar low and Iceland is absent. This is replaced in the simulation by broken convective cloud. In Figure 3(a, e), integrated WVP shows good agreement

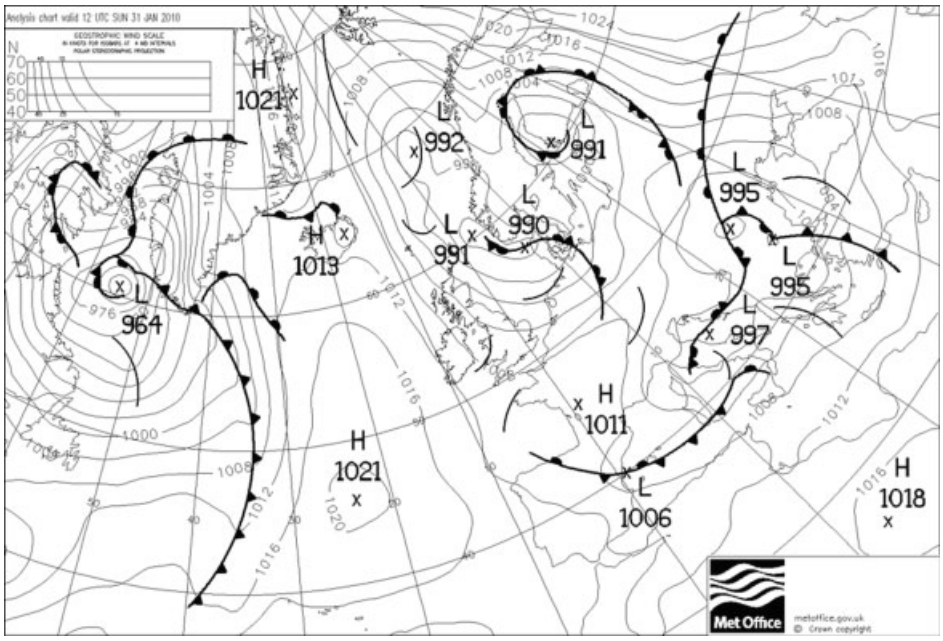

Figure 1. Analysis chart for 1200 UTC on 31 January 2010.

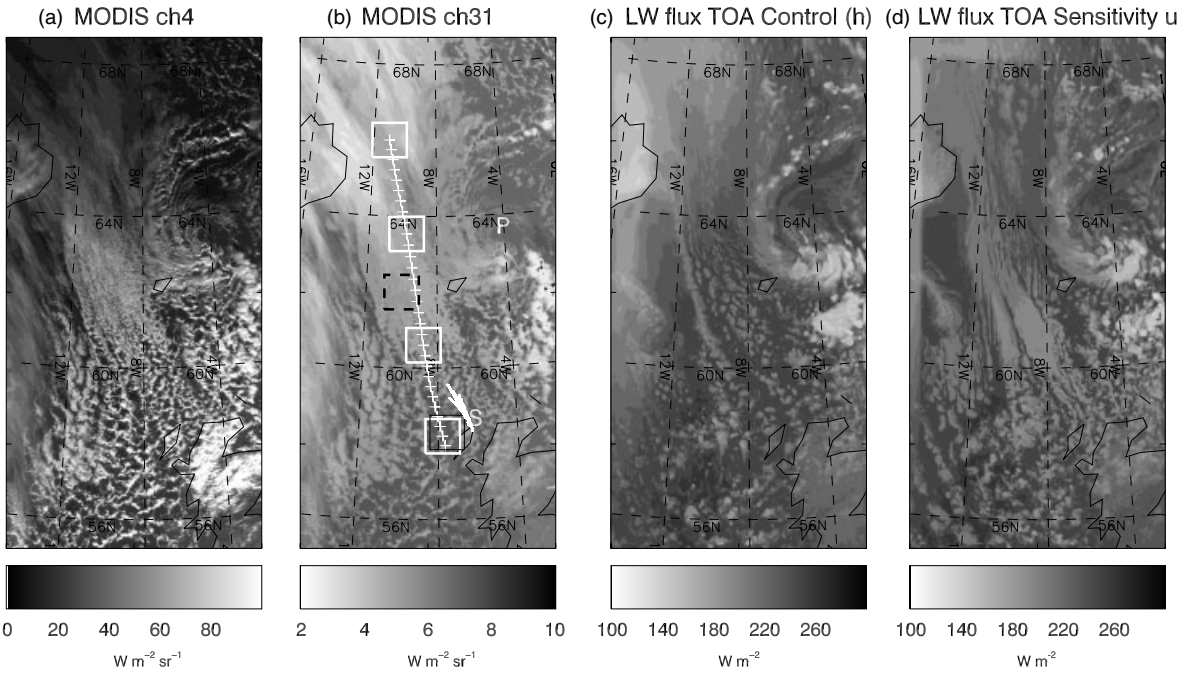

Figure 2. Comparison at 1200 UTC on 31 January 2010 of (a) MODIS channels 4 (visible, 550 nm) and (b) 31 (infrared, 10 μm) (both W m^{-2}sr^{-1}) with (c) outgoing LW from the control model (dims**h**) and (d) the sensitivity experiment (dims**u**) (both W m^{-2}). (b) contains the polar low feature indicated by a white 'P'. The sonde positions are very close to each other and are marked by a white 'S'. The aircraft runs used here are marked by the white arcs. The Lagrangian trajectory is marked as a white line extending from 66°N, 11°W with + marks at 0.5 h intervals from 0000 to 1500 UTC. White boxes indicate the locations of the Lagrangian boxes used for Figures 8 and 9. The solid black box indicates the region used for comparison with the aircraft data. The dashed black box indicates the region over which the MODIS retrievals of droplet number, cloud-top temperature/pressure and cloud water path were averaged.

between model and observations, with the polar low feature drawing in dry air from the north clearly visible. Figure 3(b) shows the LWP from AMSR-E peaked to the west of the Faroe Islands with a value of 0.3 kg m^{-2} extending towards Iceland. Outside of this region, the LWP values are 0.05 kg m^{-2} in the regions of low cloud to the north and the convective cloud region to the south. The control model exhibits very little liquid water compared with the observations (Figure 3(b, f)). The largest values are associated with the polar low feature and the deeper convection towards the southern part of the domain. Top-of-atmosphere outgoing LW radiation from the model is too great, indicating that there is not enough cloud, leaving the LW flux to be strongly affected by emission from the surface (Figure 3(c, g)). The top-of-atmosphere outgoing SW flux is affected in the northeast of the domain by the terminator, but it is still clear that the lack of cloud cover in the stratiform region means that the SW flux at the top of the atmosphere is reduced compared with the observations (Figure 3(d, h)).

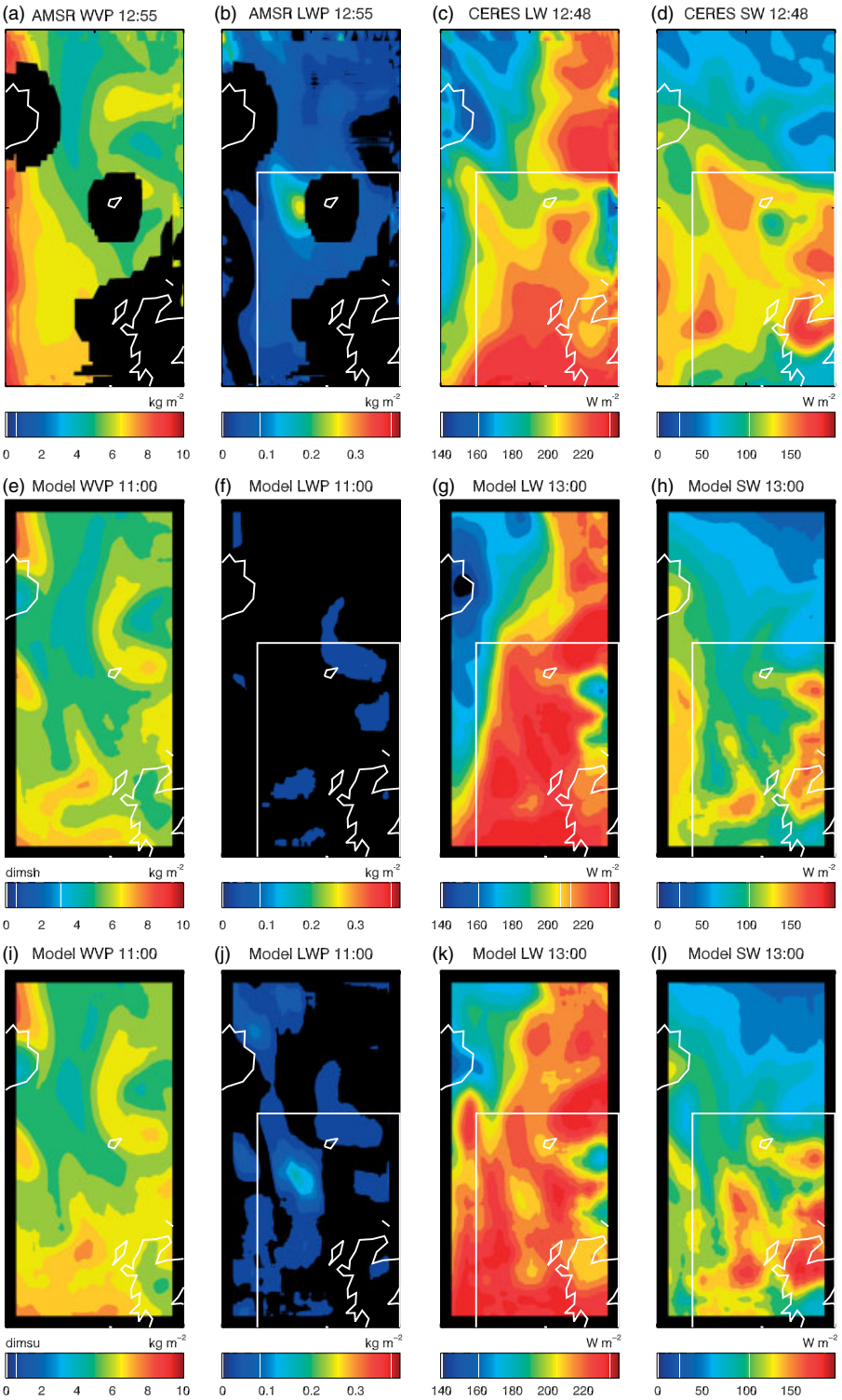

Figure 3. Comparison of (a)–(d) satellite data with (e)–(h) the control (dims**h**) model and (i)–(l) the sensitivity experiment (dims**u**). (a, e, i) show the integrated water vapour column, (b, f, j) the liquid water path, (c, g, k) the long-wave flux at the top of the atmosphere, and (d, h, l) short-wave flux at the top of the atmosphere. All data have been smoothed by a 100 km top-hat function. Black indicates a zero value or missing data. The white box indicates the region used to derive the average values presented in Table 2.

Averaging MODIS level 2 retrievals over a 100 km box centred on 62°N, 10°W (Figure 2(b)) indicates a cloud water path of $0.3 \pm 0.2\,\mathrm{kg\,m^{-2}}$ (in agreement with the microwave retrieval) and cloud-top temperature and pressure of $-14 \pm 2\,^{\circ}\mathrm{C}$ and 760 ± 30 mb for the stratiform cloud in this region. Assuming a surface pressure of 1004 mb, cloud-top height is then 2180 ± 300 m. Finally, following Boer and Mitchell (1994), the retrieved droplet effective radius and optical thickness can be combined to obtain an effective droplet concentration. The value obtained is $110 \pm 160\,\mathrm{cm^{-3}}$. An error of a factor of 10 in optical thickness would lead to an error in concentration of a factor of ~3. The lack of stratiform cloud in the control model at this location means that no meaningful comparisons can be made between the control model and the MODIS-derived values.

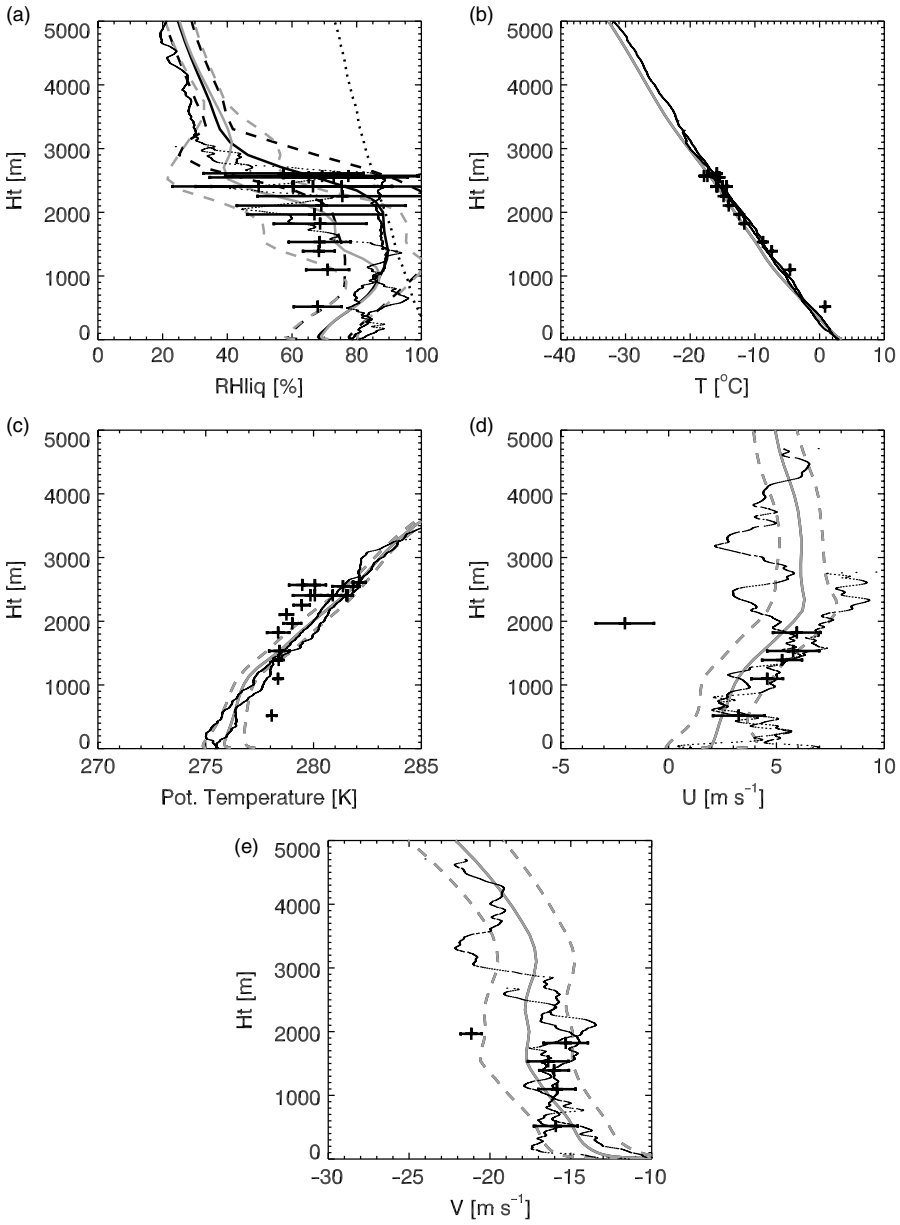

Figure 4. Height profile comparisons of dropsonde (dots) and aircraft data (+ with variability bar) with control model (**h**) data (grey lines) and sensitivity experiment (**u**) data (black lines), averaged over the 100 km×100 km box indicated in Figure 2(b). Solid lines denote the mean and dashed lines (control only) the ±1 standard deviation. If only the grey solid line is visible, then the control and sensitivity profiles are coincident. (a) Relative humidity with respect to liquid (the bold dotted line represents ice saturation), (b) temperature, (c) potential temperature, (d) *u* wind, and (e) *v* wind. Model data are at 1100 UTC, aircraft data 1100–1400 UTC.

4.1.3. Aircraft comparison

Model comparisons have been carried out by coarse-graining the model fields into 100 km squares and then comparing mean and standard deviations to the aircraft observations. In-cloud statistics were computed using grid boxes only where the condensed water mixing ratio exceeded 10^{-8}kg kg^{-1}. The fraction of grid boxes at each height exceeding this threshold within a 100 km×100 km box is called the cloud fraction. A square region centred on 8°W, 58°N was chosen for comparison with the observations based on the region where the aircraft had flown, and by assessing how well the relative humidity, temperature and horizontal wind profiles matched the observed values (this region is displaced ∼50 km southwest of where the aircraft flew). The control model is able to reproduce the horizontal winds and temperature profiles, but is not able to capture the large humidity values observed by the aircraft and dropsondes between 2000 and 2700 m.

In situ evidence for a lack of liquid water was provided from the aircraft measurements. The FAAM BAe-146 research aircraft penetrated cumulus clouds from 1000 to 1500 UTC in a region approximately bounded by 8–6°W and 58–60°N in a series of ∼50 km straight and level runs through the cumulus cloud. Downward-looking LIDAR from runs carried out at an altitude of 6 km indicated cloud top at 3.7 km. Cloud base was observed to be at 1 km. Precipitation was observed to be reaching the surface and the freezing level was at 0.5 km. One cell was followed up from 2 km, where it was mixed-phase, to 3 km, where it had completely glaciated. The clouds were observed to have liquid cores with ice outflows. Figure 4 shows vertical profiles of humidity, temperature, potential temperature and horizontal winds from two dropsondes launched by the

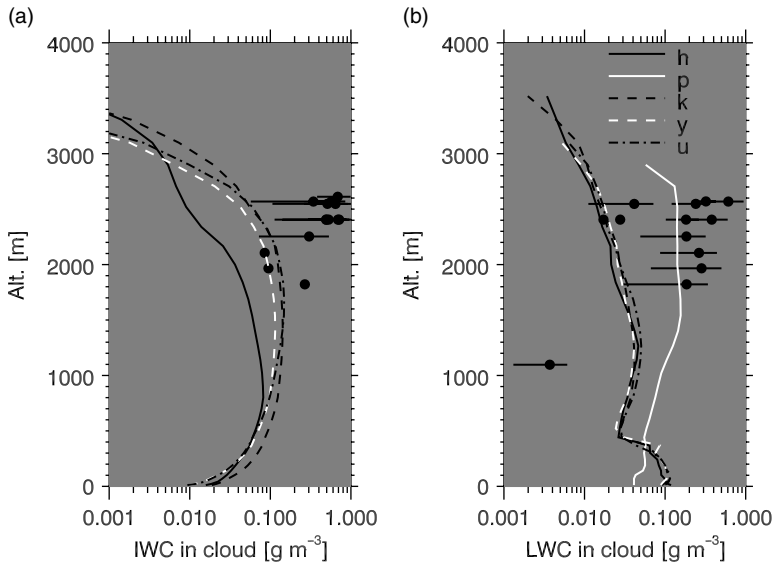

Figure 5. Height profile comparison of aircraft data (solid circles with 1 standard deviation variability bars) with 100 km × 100 km mean profiles for a subset of different configurations of the model (Table 1, **h** is control): (a) in-cloud ice water contant, (b) in-cloud liquid water content, (c) ice cloud fraction, and (d) liquid cloud fraction.

aircraft at 1037 and 1422 UTC and aircraft measurements from straight and level legs between those times (mean and one standard deviation shown). Relative humidity from the aircraft exhibits large variability encompassing the dropsonde data and ice saturation between 2.0 and 2.6 km (Figure 4(a)). Temperature from the aircraft shows good agreement with the sondes between 1.5 and 2.6 km, and the freezing level is indicated to be between 200 and 500 m (Figure 4(b)). Potential temperature shows that the aircraft-derived values exhibit less variation with height than the sondes (Figure 4(c)). Horizontal winds are available from the aircraft only up to 2 km; icing of the pitot tubes affected measurements above this altitude. Again, the aircraft measurements compare well with the dropsonde values indicating a 14–17 m s^{-1} northerly and 2–6 m s^{-1} westerly between 500 and 2000 m altitude (Figure 4(d, e)).

In-cloud condensed water estimates from the Nevzorov (IWC) and CDP (LWC) show that clouds were sampled between 1.5 and 2.6 km (Figure 5). Mean in-cloud IWC and LWC increased with altitude up to 0.7 and 0.6 g m^{-3}, respectively. Some low values of LWC can be seen near 2.5 km, indicating that the cloud had become almost completely glaciated. Greater values at the same altitude indicate that it was also the case that some clouds were not yet glaciated. LWC and IWC values measured by the aircraft were generally comparable in magnitude. Droplet concentrations measured by the CDP have mean values of 10 cm^{-3} with no obvious height dependency (Figure 6(a)). Inspection of cloud thickness, fraction and in-cloud LWC (Figure 5) suggest a LWP of ∼0.05 kg m^{-2}, consistent with the microwave-based satellite retrieval for this region. Ice with maximum dimensions greater than 100 μm exhibited concentrations which increased with height to mean concentrations of 20 l^{-1} at 2.6 km (Figure 6(b)). The greatest mean in-cloud concentration at this altitude ($T = -18\,^{\circ}$C) was 50 l^{-1}. The averaging in-cloud lengths for each run was typically 10–20 km for ice and 1–10 km for the liquid regions, reflecting the smaller extent of supercooled liquid water. Thresholds of 2 cm^{-3} and 0.01 l^{-1} on the CDP and 2D-C, respectively, were used as thresholds for computing liquid and ice in-cloud water contents.

In-cloud IWCs for the control model (black solid line, Figure 5(a)) are below the lowest measured values. We note that the measured IWC values are close to the upper limit of the Nevzorov probe and therefore IWC values may be greater than depicted. Similarly, the LWC from the control model is well below the observed values (Figure 5(b)), and ice and liquid cloud fraction are low for the control model when compared to the aircraft estimates (not shown). The model assumes a drop concentration of 100 cm^{-3} and so does not feature on Figure 6(a). Comparison of ice concentration for particles larger than 100 μm (Figure 6(b)) indicates that the simulations using the control model representation diagnose ice concentrations similar to the measured values. Microphysical process rates can be expressed in terms of the moments of the ice particle size distribution (PSD), $N(D)$, where the nth moment is defined as

$$M_n = \int D^n N(D) \mathrm{d}D.$$

In terms of microphysical processes, the diffusional growth is approximately determined by the first moment of the size distribution*. For the control representation, the first moment for particles larger than 100 μm is again in agreement with the observations from the aircraft (Figure 6(c)). Because radar reflectivity is proportional to the square of the mass of a particle and in turn the mass is approximately proportional to the square of the size, the fourth moment of the ice size distribution is proportional to the radar reflectivity. It can be seen in Figure 6(d) that the control model underpredicts the aircraft-derived values.

4.1.4. *Radar comparison*

Convective cell identification, using a 10 dBZ threshold, and tracking were used to ascertain convective cell lifetime

*Ventilation effects will lead to diffusional growth being proportional to a higher-order moment between 1 and 2.

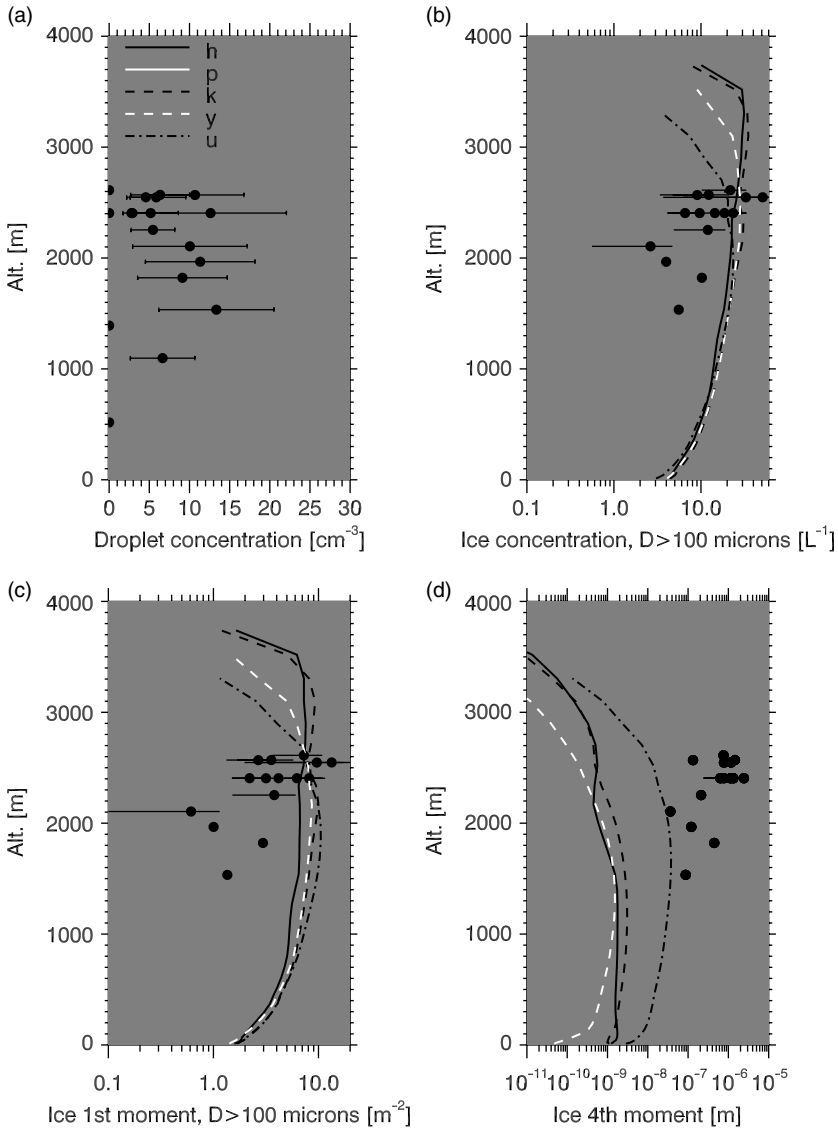

Figure 6. As Figure 5, but for (a) droplet concentration, (b) ice crystal concentration (D>100 μm, using the 2D-C), (c) first moment of ice size distribution (D>100 μm, using the 2D-C) and (d) fourth moment of ice size distribution (D>100 μm, using the CIP-100).

and size. Mean convective cell lifetime from the radar was 69 min (3 min standard error) compared to 65 min (6 min standard error) for the control. Histograms of convective cell size (Figure 7(a)), fill fraction (Figure 7(b)) and maximum reflectivity in a convective cell (Figure 7(c)) are shown. The control model (**h**) exhibits larger convective cell sizes and the fill fraction derived from the model was greater than the value derived from the radar data. Thus the convective cells derived from the model appear rounder than they are in the observations. Histograms of maximum reflectivity within a convective cell at this altitude indicates that the control model has a similar distribution of reflectivity values to the radar data.

4.1.5. *Summary of control model performance*

From comparison with aircraft, radar and satellite data several problems have been identified with the control model for this case:

(i) There is too little condensed water. In particular, the LWC is too low, and hence LWP, in both the stratiform region and the convective region, is underpredicted.
(ii) The cloud cover in the stratiform region is too broken.
(iii) The reflected SW (emitted LW) at the top of the atmosphere is too small (great), which is likely to be the result of the combination of points (i) and (ii).
(iv) In the convective region, the fourth moment of the ice size distribution is underpredicted, suggesting that the ice size distribution is too narrow.
(v) The convective cell sizes for the control model are too large and the model-derived fill fractions are too high.

4.2. *Sensitivity tests*

Shortcomings in the control model motivated a number of variations to the physics representation. These changes are described here and the different model configurations combining these changes are given in Table 1.

4.2.1. *Shear-dominated boundary layer*

This change was motivated by the lack of stratiform cloud between the polar low and Iceland. As described in section 3, the boundary layer scheme in the UM provides a diagnosis of boundary-layer 'type' based on the surface buoyancy

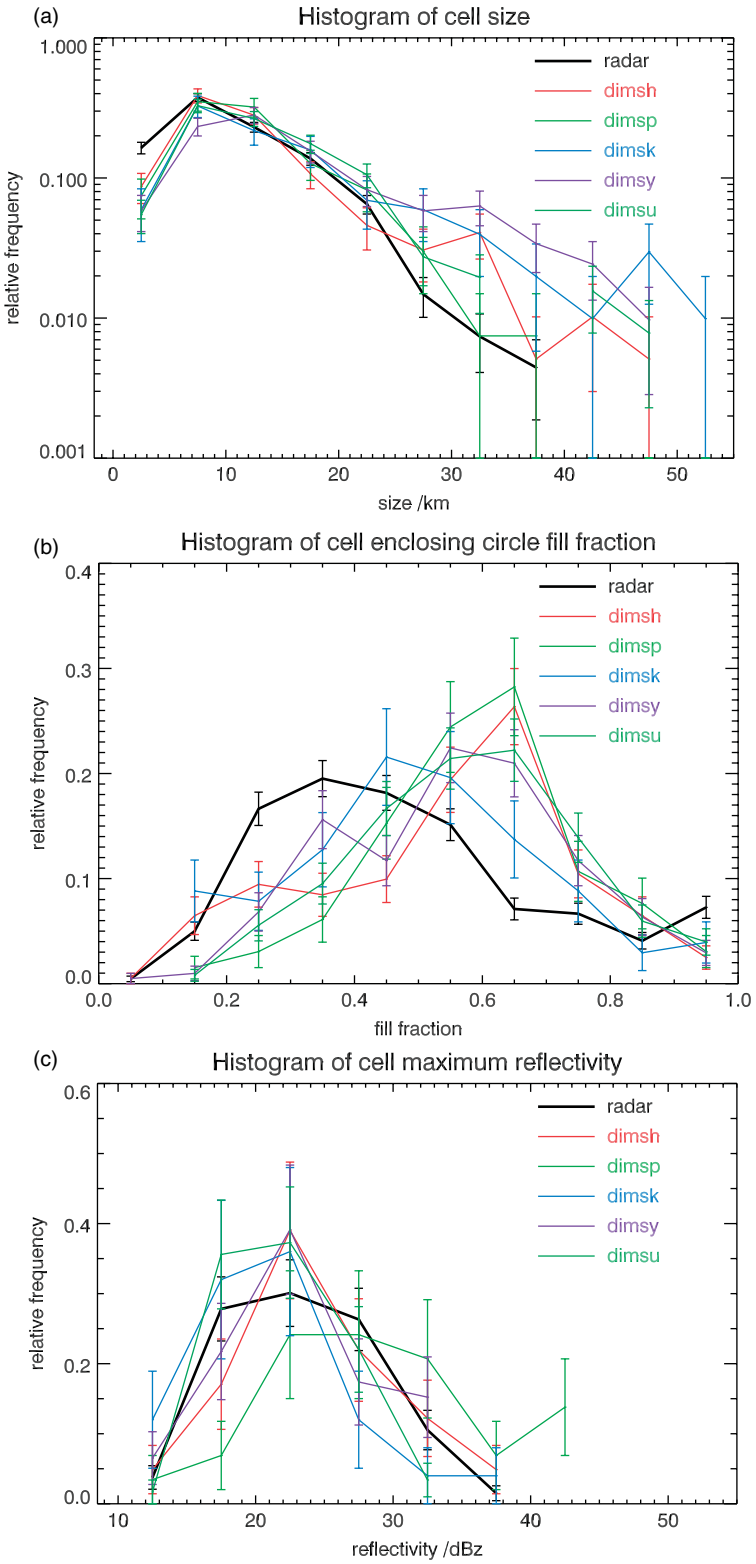

Figure 7. Comparison of convective cell statistics (mean and standard deviation) for a 10 dBZ radar reflectivity contour at 2 km altitude derived from the control (**h**) and a subset of sensitivity experiment model and radar data: normalised histograms of (a) convective cell size, (b) convective cell fill fraction, and (c) maximum reflectivity in a cell.

flux and the thermodynamic profile characteristics which determine the non-local mixing throughout the boundary layer. If the environment is diagnosed to be conditionally unstable, then vertical mixing is assumed to be resolved and the boundary-layer scheme does not handle the mixing above the lifting condensation level. This was the case in the control model and meant that it was difficult to achieve the 100% cloud cover in the stratiform region indicated by the satellite observation. It was hypothesised that the large vertical shears experienced in these regions were not being dealt with properly. Shear generation of turbulence can extend mixing into regions of weak static stability. To allow for this effect, additional dynamical constraints were added which can allow the boundary-layer scheme's

Table 1. Model variations. For brevity in the text, the different configurations are referred to by their last letter. The control model is dims**h**.

Experiment	Shear-dom. BL	$T_{nuc} = -18\,^{\circ}C$	$AcE = 0.1$	No ice	PSD	3d Smag
dims**h**	–	–	–	–	–	–
dims**p**	–	–	–	✓	–	–
dims**q**	–	–	✓	–	–	–
dims**n**	–	–	–	–	–	✓
dims**k**	✓	–	–	–	–	–
dims**i**	✓	–	✓	–	–	–
dims**z**	✓	✓	–	–	–	–
dims**y**	✓	✓	✓	–	–	–
dims**u**	✓	✓	✓	–	✓	–
dims**w**	–	✓	✓	–	–	✓

non-local diffusion profiles to parametrize the mixing right up to cloud top. This diagnosis is made by inspection of the local Richardson number profile: if this is less than 0.25 from the surface to at least the mid-point of the cloud layer, then wind shear is assumed to disrupt the formation of cumulus clouds and the boundary-layer scheme diagnoses a more appropriate well-mixed stratocumulus-topped boundary layer (Bodas-Salcedo *et al.*, 2012, give additional details).

4.2.2. $T_{nuc} = -18\,^{\circ}C$

The lack of liquid water in the control model led to the hypothesis that the production of ice was too efficient. Currently, in common with other operational microphysics schemes, the model produces ice through heterogeneous freezing when the temperature is $-10\,^{\circ}C$ or lower and liquid water is present. This represents a condensation or immersion freezing mechanism. Changing the primary heterogeneous ice nucleation temperature T_{nuc} from -10 to $-18\,^{\circ}C$ inhibited ice production until the boundary-layer top approached about 4 km. Using a lower heterogeneous freezing temperature is supported by both laboratory and remote-sensing observations (Field *et al.*, 2006; Ansmann *et al.*, 2008; Westbrook and Illingworth, 2011). In addition to the nucleation temperature change, no ice below 4 km was allowed to enter through the boundaries. Any ice entering the boundary or in the initial model fields was converted to liquid water. This was done to avoid contamination by ice from the coarser nest domains and initial fields without having to rerun the entire suite. It is noted that, for these ice inhibition sensitivity experiments, the upper-level cirrus will not fully recover during the course of the simulation because of the initialisation.

4.2.3. *No Ice*

A more extreme inhibition of ice formation. All the ice processes were eliminated and any existing ice in the initial conditions was converted to liquid (including a latent heat correction).

4.2.4. *AcE=0.1*

The lack of liquid water led to the hypothesis that the production of precipitation through autoconversion was too efficient. The operational UM uses the Tripoli and Cotton (1980) formulation of autoconversion. The autoconversion efficiency, *AcE*, is usually set to 0.55, but for this sensitivity experiment the value was changed to 0.1 to reduce the transfer of cloud water to precipitation.

Table 2. Model biases. Mean of (experiment−observations) from box depicted in Figure 3.

Experiment		LWP ($kg\,m^{-2}$)	SW ($W\,m^{-2}$)	LW ($W\,m^{-2}$)
	Obs. mean	0.042	135	214
dims**h**		−0.029	−22	11
dims**p**		0.101	2	1
dims**q**		−0.030	−22	12
dims**n**		−0.030	−13	6
dims**k**		−0.028	−8	5
dims**i**		−0.029	−8	5
dims**z**		−0.021	−10	6
dims**y**		−0.017	−9	5
dims**u**		−0.014	−8	7
dims**w**		−0.019	−10	5

4.2.5. *3d Smag*

It was hypothesised that water may be mixed more efficiently throughout the boundary layer if the model were able to do the mixing explicitly. Instead of using the boundary-layer scheme to do the vertical mixing, local explicit mixing using the Smagorinsky approach (1963) was used (asymptotic mixing length 375 m).

4.2.6. *PSD*

The aircraft observations showed that some properties of the ice/snow size distribution were not well represented (the UM has a single prognostic to represent ice and aggregates of ice/snow). The ice/snow representation was changed from the standard exponential representation (Wilson and Ballard, 1999) to one which was derived from a more extensive range of aircraft observations (Field *et al.*, 2007).

4.3. *Comparison with sensitivity tests*

4.3.1. *Satellite comparison*

Table 2 contains sub-domain averages for the different experiments, restricted to the bottom right of the domain (east of 12°W and south of 64°N; Figure 3) to exclude the cirrus cloud affected by initialisation for the ice-inhibited sensitivity experiments. For the LWP, reducing the

occurrence of ice had the greatest effect. The total removal of ice processes (**p**) produced LWP values of a similar magnitude to the satellite observation in the stratiform and convective region, but produced very unrealistic results around the polar low feature (not shown), resulting in a positive mean bias. The change in the heterogeneous freezing temperature (**k,z**) increased the LWP in the stratiform region but not as much as removing all ice processes. Reducing the autoconversion on top of the freezing temperature change (**z,y**) also increased LWP slightly further. Changing the ice PSD allowed more supercooled liquid water to persist (**y,u**). SW and LW flux biases in Table 2 show improvement when the shear-dominated boundary layer was used (**h,k**). Combining $T_{\mathrm{nuc}} = -18\,^{\circ}\mathrm{C}$ with the shear-dominated boundary layer did not lead to further significant improvements. The *No ice* experiment seemed to remove the bias in SW and LW, but this is because overly bright cloud associated with the polar low feature compensated for the stratiform region being too dim. Finally, it is noted that the assumed droplet number of $100\,\mathrm{cm}^{-3}$ is in agreement with the retrieval from MODIS, but it is greater than was observed in the convective cloud. Changing to a lower concentration will decrease the SW at the top of the atmosphere back towards the control values. However, the underestimate of the liquid water and cloud fraction by the model are the dominant factors for the radiation.

Changes to the model physics representations led to improved cloud cover, LWPs and associated radiative fluxes. However, while the sensitivity experiments which involve changes to the boundary layer (all apart from **h,q**) produce improved SW and LW results, it is difficult to decide between these, given the uncertainty in the observed values. Sensitivity experiment **u**, which included the PSD change, did better with the LWP and, as will be seen, the characteristics of the ice size distribution within the convective cloud. Additional changes to assumptions within the SW radiation scheme could further reduce these biases, but the first-order change to the SW response is associated with the increase in stratiform cloud cover. It has been decided to give greater weight to the improvements to LWP than those to the radiation and, therefore, the comparisons shown in Figures 2, 3, 4, 8, 9 (to be discussed next) show results from the control model **h** and the favoured sensitivity experiment **u**.

Figure 3 shows comparisons of the **u** model from Table 1 with satellite-derived LWP, top-of-atmosphere SW and LW fluxes. All of the fields are smoothed with a 100 km top-hat filter. As before, the integrated water vapour path fields (Figure 3(a, i)) are similar, but now the LWP exhibits much greater values with a peak exceeding $0.2\,\mathrm{kg\,m}^{-2}$ (Figure 3(j)). Increases in cloud fraction mean that the LW flux (Figure 3(k)) is reduced relative to the control model (Figure 3(g)) and is closer to the satellite-derived value. The increased cloud cover leads to increased SW flux (Figure 3(h, l)) relative to the control model.

The presence of extensive stratiform cloud at 62°N, 10°W allows a comparison to be made between the model fields and the MODIS retrievals. For the **u** sensitivity experiment, the mean values obtained for the 100 km × 100 km box (with standard deviations in brackets) compared with the MODIS values are shown in Table 3.

Table 3. Mean values over a 100 km × 100 km box (with standard deviation in brackets).

Variable	From **u** experiment	From MODIS
Cloud-top temperature (°C)	−16 (1)	−14 (2)
Cloud-top pressure (mb)	770 (20)	760 (30)
Cloud-top height (m)	1970 (180)	2180 (300)
LWP ($\mathrm{kg\,m}^{-2}$)	0.15 (0.1)	0.30 (0.2)

4.3.2. *Aircraft comparison*

Inhibiting ice production to lower temperatures is required to increase the model LWC. Only the experiment where ice has been switched off (**p**) approaches the observed LWCs (Figure 5(b)); when ice is present it inhibits the liquid in the stratiform cloud and elsewhere. The contrast between the good agreement between the predicted and measured ice properties in this convective region and the difficulties with reproducing the LWC leads to the suggestion that, when liquid and ice are present in a grid box, there is not enough physical separation of these two phases. i.e. the two phases are assumed to be well-mixed throughout a grid box and in contact via the vapour phase for the Wegener–Bergeron–Findeisen mechanism to operate and they are able to collide with each other. Both these processes efficiently remove the liquid phase from the grid box.

The boundary-layer changes increase both in-cloud IWC (Figure 6(a); **k,y,u**) and ice fraction (not shown) to values comparable to the observations, even though the impact of that change is far upstream. Comparison of ice concentration and the first moment of the ice size distribution for particles larger than 100 μm indicates that the simulations using the standard representation (Figure 6(b, c); **h,k,y**) diagnose values comparable to the observations. The new PSD representation produces better agreement with the fourth moment of the ice size distribution (Figure 6(d)), indicating that the observed PSD was much broader than the control model representation for this case.

4.3.3. *Radar comparison*

For simplicity, only a subset of the results have been shown. Comparing convective cell sizes (defined by the 10 dBZ reflectivity contour) shows that most experiments exhibit greater frequencies of larger convective cell sizes (>20 km) than the radar (Figure 7(a)). Experiments (**h,q**), (**k,i**), (**z,y**) differ through the change to the autoconversion and result in increases in the occurrence of convective cells with greater fill fractions (not shown). Looking at the effect of inhibiting the ice production process experiments (**h,p**) and (**k,z**) (not shown) indicate that the convective cell sizes tend to decrease and the maximum reflectivities increase. Experiments (**k,n**), (**y,w**) show little change when Smagorinsky mixing is used in the vertical. Changing the ice PSD (**y,u**) resulted in smaller convective cell sizes and decreased occurrence of maximum reflectivity greater than 30 dBZ.

4.3.4. *Lagrangian profiles*

It is easier to understand how the boundary layer is evolving by tracking a region in an approximately Lagrangian way. A region was advected with a mean model wind (averaged

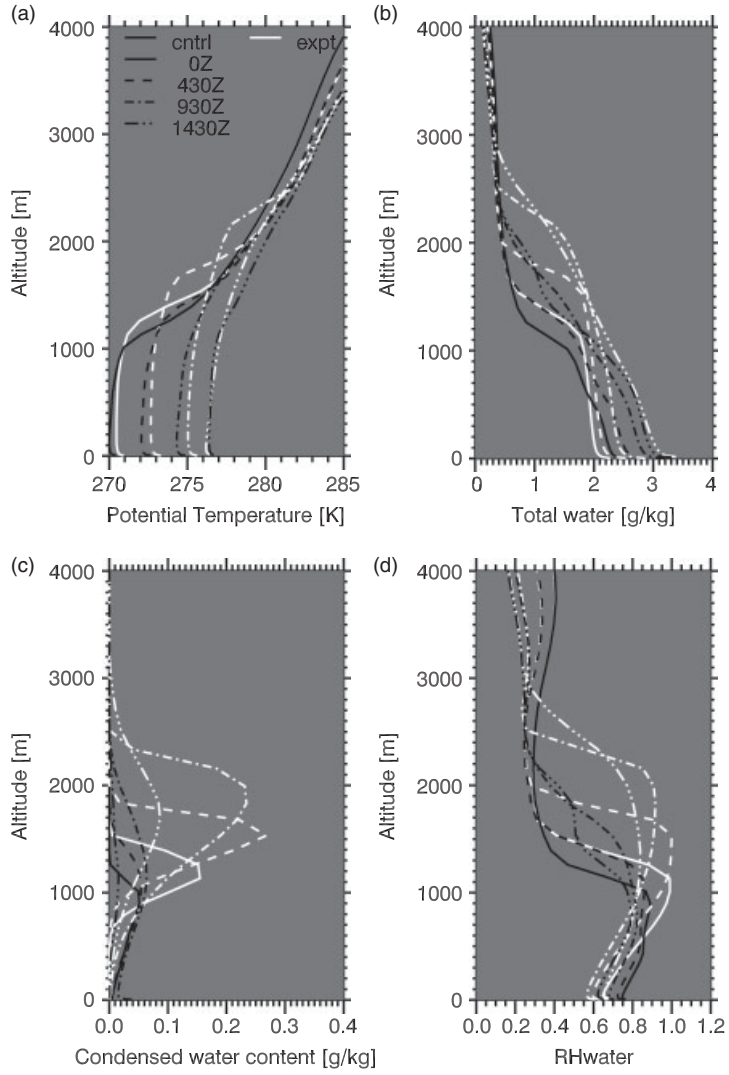

Figure 8. Boundary-layer profiles comparing the control model (**h**) and one of the sensitivity experiments (**u**) at four times along the quasi-Lagrangian trajectory highlighted in Figure 2(b): (a) potential temperature, (b) total water, (c) condensed water content, and (d) relative humidity with respect to liquid.

below 1.5 km) within a 100 km × 100 km domain, by simple forward stepping in time, from 66°N, 11°W at 0000 UTC to 57°N, 6°W at 1500 UTC (Figure 2(b)). Inspection of model profiles within the stratiform part of the cloud at 0430 UTC (not shown) provides an assessment of the impact of the sensitivity experiments. The experiments which differ only by the change in autoconversion ((**h,q**), (**k,i**), (**z,y**)) do not exhibit much change in liquid fraction or LWC. The shear-driven boundary layer change (**h,k**) leads to increased liquid cloud fraction but not increased LWC. When the ice processes are switched off or inhibited ((**h,p**), (**k,z**)) the LWC and fraction are greatly increased. For both the switching off of ice and the change to the boundary-layer mixing, the net flux of moisture through the cloud base will increase. Using *3d Smag* ((**k,n**), (**y,w**)) also leads to increases in both liquid cloud fraction and content, but not to the same extent as ice inhibition. The *3d Smag* experiments also gives rise to a lower boundary-layer top than those using the shear-dominated boundary layer, probably due to the poor resolution leading to less efficient entrainment.

Mean vertical profiles (Figure 8) show the boundary layer growing from 1.5 km at 0000 UTC to 3 km at 1430 UTC. The control (**h**) has a lower boundary-layer top and exhibits less well-mixed profiles of potential temperature and total water than the favoured sensitivity experiment shown (**u**). This results in drier profiles (Figure 8(d)), lower cloud fractions (Figure 9), and less condensed liquid water (Figure 8(c)) than the experiment. The effect of changing the treatment of the boundary layer either through the shear-dominated boundary layer or using *3d Smag* (not shown) for the vertical mixing was to create a more well-mixed boundary layer, evident in the potential temperature and total water plots (Figure 9(a, b)). The relative humidity profiles for the experiment are much closer to water saturation (also Figure 4(a)) and condensed water amounts are increased. Time evolution of the liquid and ice cloud fraction shows that the experiment is able to evolve from 100% liquid cloud cover at an early stage to greater fractions of ice cloud later (Figure 9). In contrast, the control model exhibits generally decreasing ice and liquid cloud fraction with time.

5. Discussion

Stratiform cloud poleward of the open cellular convection is a common feature of cold air outbreaks (e.g. Brümmer and Pohlmann, 2000). The lack of this cloud in the control 1.5 km

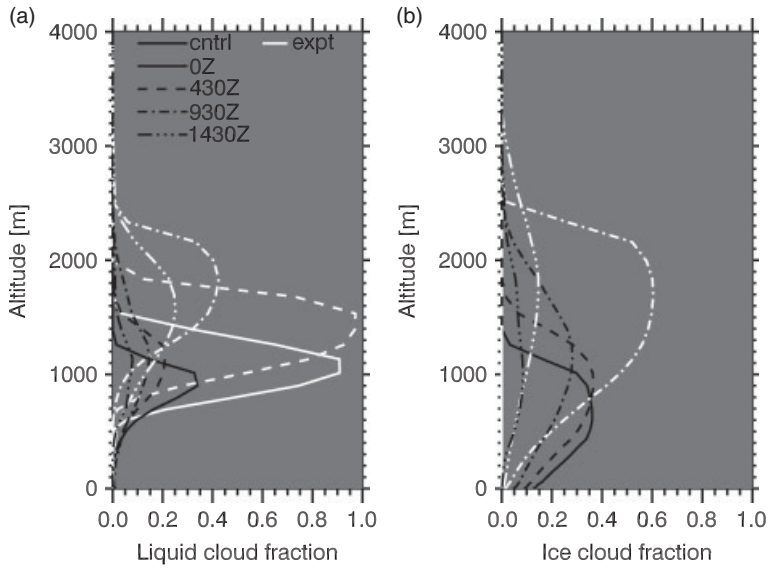

Figure 9. As Figure 8, but for (a) liquid cloud fraction and (b) ice cloud fraction. Cloud fraction is the fraction of grid boxes within the 100 km × 100 km box at each height which contain more than 10^{-8} kg kg^{-1} of condensed water. Comparison of control model (**h**) with sensitivity experiment (**u**).

run highlights the difficulty even convection-permitting models have with representing cloud systems with shallow boundary layers. The modification of the boundary-layer scheme to recognize that a shear-dominated boundary layer will result in a stratocumulus-topped boundary layer led to an improved representation in terms of cloud coverage and outgoing top-of-atmosphere SW flux. This change also allowed the model to capture the transition from stratiform cloud to open-celled convection. Such an approach was also implemented in a global model, leading to better representation of this cloud type around midlatitude cyclones (Bodas-Salcedo *et al.*, 2012). However, even with the boundary-layer modification, the LWP from the model was much smaller than that estimated from the satellite retrieval. Model-derived LWPs only approached similar values to those reported by the satellite measurements when the temperature at which ice was produced by heterogeneous freezing was lowered from −10 °C to −18 °C. This meant that ice did not form until the boundary layer had grown towards 4 km and the cloud had broken up into cellular convection. For this case, even the reduction in the ice production was not sufficient to match the aircraft observations of supercooled LWC. Only an unrealistic suspension of ice processes (*No Ice*) was able to produce LWC profiles which matched the aircraft observations.

The improvement of LWC through the inhibition of ice processes is a result reported by others (e.g. Klein *et al.*, 2009) and has implications for other microphysics schemes which use a heterogeneous ice onset temperature around − 10°C. However, the simple setting of the freezing onset temperature in the operational UK model to −18 °C may have adverse consequences, due to the lower precipitation efficiency of shallow wintertime showers, and needs to be tested further. The lower onset temperature may just be a result of a rarer occurrence of ice nuclei in air from the Arctic than airmasses arriving from Europe. This proposition provides motivation for testing cold air outbreak cases with an aerosol–cloud interactive NWP suite.

The LWCs were still too low for the sensitivity test with the modified boundary layer, lower freezing temperature and modified PSD (**u**). This raises the possibility that the well-mixed assumption between liquid and ice phases is not correct. In the Unified Model, there is a cloud phase overlap which determines how efficient riming and the Wegener–Bergeron–Findeisen process will be. For this modelled case, the ice and liquid phases are in maximum contact through the vapour phase and the potential to rime. The *No Ice* test shows that, if it were possible to shield the liquid phase from the ice phase within a grid box, then the correct LWPs could be generated for the stratiform and convective cloud region, but not the polar low feature. More work needs to be done on determining how to parametrize the mixed-phase characteristics at the grid-scale in these convection-permitting models. It is clear that updraughts greater than a few metres per second will be sufficient to lead to a plume of liquid-only cloud surrounded by ice. It may be possible to use high-resolution (decametre grid spacing) cloud-resolving model studies to help derive a parametrization to represent this behaviour.

Modifying the boundary-layer scheme to recognise a shear-dominated boundary layer and decreasing the heterogeneous freezing temperature produced model results which improved upon those from the control model for SW and LW fluxes. The sensitivity experiment (**u**), which included the change to the ice PSD, also improved the LWP and characteristics of the ice size distribution within the convective cloud. Because of the assumptions in the radiation scheme, more weight was given to the quantitative improvements in LWP and *in situ* aircraft observations. The (**u**) configuration which incorporated the modified boundary-layer scheme, the change in the onset of heterogeneous freezing to lower temperatures, the reduction in autoconversion efficiency, and the new snow PSD, was felt to produce the best simulation. Figure 2 shows a comparison of LW flux at the top of the atmosphere from the original control model (**h**), the MODIS infrared channel and the (**u**) sensitivity experiment, noting that the lack of cirrus is due to the initialisation used for this experiment.

6. Conclusions

From this study we can draw the following conclusions for the representation by a 1.5 km model of cold air outbreaks.

(i) The favoured sensitivity experiment (**u**) evolves a shallow boundary-layer stratiform cloud into a deeper boundary layer with open cellular convection producing better agreement with the observations than the control model.
(ii) Using a non-local mixing boundary-layer scheme to implicitly represent a shear-dominated boundary layer as a stratocumulus-topped layer appears successful. This treatment reproduces the ∼100% cloud cover exhibited by the stratus layer and enhances the SW TOA flux.
(iii) A temperature of −10 °C for the onset of ice formation is too high. This is presumably because of the clean nature of the airmass originating in the Arctic and the lack of efficient ice nuclei available. A lower temperature onset for heterogeneous ice production improved liquid water contents.
(iv) The model representation of the mixed phase is too efficient at removing liquid.

Acknowledgements

We thank the crew and personnel at NERC/Met Office/DirectFlight for the operation of the FAAM BAe-146 during the CONSTRAIN campaign. We would like to thank the two anonymous referees for providing comments which helped improve this article. Use was made of satellite products provided by NASA and Remote Sensing Systems (http://www.ssmi.com/).

References

Ansmann A, Tesche M, Althausen D, Müller D, Seifert P, Freudenthaler V, Heese B, Wiegner M, Pisani G, Knippertz P, Dubovik O. 2008. Influence of Saharan dust on cloud glaciation in southern Morocco during the Saharan Mineral Dust Experiment. *J. Geophys. Res.–Atmos.* **113**: D4, D04210. DOI: 10.1029/2007JD008785.

Bodas-Salcedo A, Williams KD, Field PR, Lock AP. 2012. The surface downwelling solar radiation surplus over the Southern Ocean in the Met Office model: The role of midlatitude cyclone clouds. *J. Climate*: **25**: 7467–7486.

Brümmer B, Pohlmann S. 2000. Wintertime roll and cell convection over Greenland and Barents Sea regions: A climatology. *J. Geophys. Res.–Atmos.* **105**: D12, 15559–15566. DOI: 10.1029/1999JD900841.

Cotton RJ, Field PR, Ulanowski Z, Kaye PH, Hirst E, Greenaway RS, Crawford I, Crosier J, Dorsey J. 2012. The effective density of small ice particles obtained from *in situ* aircraft observations of midlatitude cirrus. *Q. J. R. Meteorol. Soc.* in press. DOI: 10.1002/qj.2058.

Cullen MJP, Davies T, Mawson MH, James JA, Coulter SC, Malcolm AJ. 1997. An overview of numerical methods for the next generation UK NWP and climate model. In *Numerical Methods in Atmospheric and Ocean Modelling: The Andre J. Robert Memorial Volume*. Lin CA, Laprise R, Ritchie H (eds). Canadian Meteorol. Oceanogr. Soc: 425–444.

Davies T, Cullen MJP, Malcolm AJ, Mawson MH, Staniforth A, White AA, Wood N. 2005. A new dynamical core for the Met Office's global and regional modelling of the atmosphere. *Q. J. R. Meteorol. Soc.* **131**: 1759–1782.

Field PR, Heymsfield AJ, Bansemer A. 2006a. Shattering and particle interarrival times measured by optical array probes in ice clouds. *J. Atmos. Oceanic Technol.* **23**: 1357–1371.

Field PR, Mohler O, Connolly P, Kramer M, Cotton RJ, Heymsfield AJ, Saathoff H, Schnaiter M. 2006b. Some ice nucleation characteristics of Asian and Saharan desert dust. *Atmos. Chem. Phys.* **6**: 2991–3006.

Field PR, Heymsfield AJ, Bansemer A. 2007. Snow size distribution parameterization for midlatitude and tropical ice clouds. *J. Atmos. Sci.* **64**: 4346–4365.

Gryschka M, Raasch S. 2005. Roll convection during a cold air outbreak: A large eddy simulation with stationary model domain. *Geophys. Res. Lett.* **32**: 14, DOI: 10.1029/2005GL022872.

Horvath A, Davies R. 2007. Comparison of microwave and optical cloud water path estimates from TMI, MODIS, and MISR. *J. Geophys. Res.* **112**: D01202, DOI: 10.1029/2006JD007101.

Karlsson J, Svensson G. 2011. The simulation of Arctic clouds and their influence on the winter surface temperature in present-day climate in the CMIP3 multi-model dataset. *Clim. Dyn.* **36**: 623–635. DOI: 10.1007/s00382-00010-00758-00386.

Klein SA, McCoy RB, Morrison H, Ackerman AS, Avramov A, de Boer G, Chen M, Cole JNS, Del Genio AD, Falk M, Foster MJ, Fridlind A, Golaz J-C, Hashino T, Harrington JY, Hoose C, Khairoutdinov MF, Larson VE, Liu X, Luo Y, McFarquhar GM, Menon S, Neggers RAJ, Park S, Poellot MR, Schmidt JM, Sednev I, Shipway BJ, Shupe MD, Spangenbery DA, Sud YC, Turner DD, Veron DE, von Salzen K, Walker GK, Wang Z, Wolf AB, Xie S, Xu K-M, Yang F, Zhang G. 2009: Intercomparison of model simulations of mixed-phase clouds observed during the ARM Mixed-Phase Arctic Cloud Experiment.. I: Single-layer cloud. *Q. J. R. Meteorol. Soc.* **135**: 979–1002.

Kolstad EW, Bracegirdle TJ, Seierstad IA. 2009. Marine cold-air outbreaks in the North Atlantic: temporal distribution and associations with large-scale atmospheric circulation. *Clim. Dyn.* **33**: 187–197. DOI: 10.1007/s00382-008-0431-5.

Korolev AV, Emery EF, Strapp JW, Cober SG, Isaac GA, Wasey M, Marcotte D. 2011. Small ice particles in tropospheric clouds: Fact or artifact? Airborne Icing Instrumentation Evaluation Experiment. *Bull. Amer. Meteorol. Soc.* **92**: 967–973.

Korolev AV, Strapp JW, Isaac GA, Nevzorov AN. 1998. The Nevzorov airborne hot-wire LWC-TWC probe: Principle of operation and performance characteristics. *J. Atmos. Oceanic Technol.* **15**: 1495–1510.

Lean HW, Clark PA, Dixon M, Roberts NM, Fitch A, Forbes R, Halliwell C. 2008. Characteristics of high-resolution versions of the Met Office Unified Model for forecasting convection over the United Kingdom. *Mon. Weather Rev.* **136**: 3408–3424.

Liu AQ, Moore GWK, Tsuboki K, Renfrew IA. 2006. The effect of the sea-ice zone on the development of boundary-layer roll clouds during cold air outbreaks. *Boundary-Layer Meteorol.* **118**: 557–581.

Liu X, Xie S, Boyle J, Klein SA, Shi X, Wang Z, Lin W, Ghan SJ, Earle M, Liu PSK, Zelenyuk A. 2011. Testing cloud microphysics parameterizations in NCAR CAM5 with ISDAC and M-PACE observations. *J. Geophys. Res.–Atmos.* **116**: DOI: 10.1029/2011JD015889.

Lock AP. 2011. 'The Parametrization of Boundary-Layer Processes'. Unified Model Documentation Paper 24. Met Office: Exeter, UK. Available at http://collab.metoffice.gov.uk/twiki/pub/Support/Umdp/024_79.pdf.

Lock AP, Brown AR, Bush MR, Martin GM, Smith RNB. 2000. A new boundary-layer mixing scheme. Part I: Scheme description and single-column model tests. *Mon. Weather Rev.* **128**: 3187–3199.

Loeb NG, Kato S, Loukachine K, Manalo-Smith N, Doelling DR. 2007. Angular distribution models for top-of-atmosphere radiative flux estimation from the Clouds and the Earth's Radiant Energy System Instrument on the Terra satellite. Part II: Validation. *J. Atmos. Oceanic Technol.* **24**: 564–584.

Morrison H, Pinto JO. 2006. Intercomparison of bulk cloud microphysics schemes in mesoscale simulations of springtime Arctic mixed-phase stratiform clouds. *Mon. Weather Rev.* **134**: 1880–1900.

McBeath K, Field PR, Cotton R. 2012. Using operational weather radar to assess high-resolution numerical weather prediction over the British Isles for a cold air outbreak case-study. *Q. J. R. Meteorol. Soc.* In Press.

O'Dell CW, Wentz FJ, Bennartz R. 2008. Cloud liquid water path from satellite-based passive microwave observations: A new climatology over the global oceans. *J. Climate* **21**: 1721–1739.

Smagorinsky J. 1963. General circulation experiments with the primitive equations. Part 1: the basic experiment. *Mon. Weather Rev.* **91**: 99–164.

Trenberth KE, Fasullo JT. 2010. Simulation of present-day and twentyfirst-century energy budgets of the Southern Oceans. *J. Climate* **23**: 440–454.

Tripoli GJ, Cotton WR. 1980. A numerical investigation of several factors contributing to the observed variable intensity of deep convection over south Florida. *J. Appl. Meteorol.* **19**: 1037–1063.

Wacker U, Potty KVJ, Lüpkes C, Hartmann J, Raschendorfer M. 2005. A case study on a polar cold air outbreak over fram strait using a mesoscale weather prediction model. *Boundary-Layer Meteorol.* **117**: 301–336. DOI: 10.1007/s10546-005-2189-1.

Walters DN, Best MJ, Bushell AC, Copsey D, Edwards JM, Falloon PD, Harris CM, Lock AP, Manners JC, Morcrette CJ, Roberts MJ,

Stratton RA, Webster S, Wilkinson JM, Willett MR, Boutle IA, Earnshaw PD, Hill PG, MacLachlan C, Martin GM, Moufouma-Okia W, Palmer MD, Petch JC, Rooney GG, Scaife AA, Williams KD. 2011. The Met Office Unified Model Global Atmosphere 3.0/3.1 and JULES Global Land 3.0/3.1 configurations. *Geosci. Model Dev.* **4**: 919–941. DOI: 10.5194/gmd-4-919-2011.

Wentz FJ, Spencer RW. 1998. SSM/I rain retrievals within a unified all-weather ocean algorithm. *J. Atmos. Sci.* **55**: 1613–1627.

Westbrook CD, Illingworth AJ. 2011. Evidence that ice forms primarily in supercooled liquid clouds at temperatures >−27C. *Geophys. Res. Lett.* **38**: L14808, DOI: 10.1029/2011GL048021.

Wielicki BA, Barkstrom BR, Harrison EF, Lee III RB, Smith GL, Cooper JE. 1996. Clouds and the Earth's Radiant Energy System (CERES): An Earth observing system experiment. *Bull. Amer. Meteorol. Soc.* **77**: 853–868.

Wilkinson JM. 2011. 'The Large-Scale Precipitation Parametrization Scheme'. Unified Model Documentation Paper 26. Met Office: Exeter, UK. Available at http://collab.metoffice.gov.uk/twiki/pub/Support/Umdp/026_77.pdf.

Wilkinson JM, Wells H, Field PR, Agnew P. 2012. Investigation and prediction of helicopter-triggered lightning over the North Sea. *Meteorol. Appl.* DOI: 10.1002/met.1314.

Wilson DR, Ballard SP. 1999. A microphysically based precipitation scheme for the UK Meteorological Office Unified Model. *Q. J. R. Meteorol. Soc.* **125**: 1607–1636.

